Pergamon

Acta mater. Vol. 46, No. 11, pp. 3949–3962, 1998

Printed in Great Britain
PII: S1359-6454(98)00048-2
1359-6454/98 $19.00 + 0.00

MODELLING OF REAUSTENITIZATION FROM THE PEARLITE STRUCTURE IN STEEL

A. JACOT[1]†, M. RAPPAZ[1] and R. C. REED[2]

[1]Laboratoire de métallurgie physique, Ecole Polytechnique Fédérale de Lausanne, MX-G, CH-1015 Lausanne, Switzerland and [2]Department of Materials Science and Metallurgy, University of Cambridge, Pembroke Street, Cambridge CB2 3QZ, U.K.

(Received 10 October 1997; accepted 6 February 1998)

Abstract—A two-dimensional model has been developed for the description of the formation of austenite from lamellar pearlite in steel. The diffusion equation is solved in a small domain representative of a regular structure of lamellar pearlite. The solution is obtained using a finite element method with a deforming mesh and a remeshing procedure. The main assumption of the model is the condition of local equilibrium at the interfaces, including the curvature contribution and mechanical equilibrium of surface tensions at the triple junction where the ferrite, austenite and cementite phases meet. The velocity of the interface is deduced from a solute balance which involves the concentration given by the phase diagram modified by the Gibbs–Thomson effect. The model is used to predict the dissolution rate, the shape of the interface as well as the concentration field in austenite as a function of temperature. Both the transient and steady-state regimes are described. The model is first applied to a model alloy whose physical properties allow the problem to be solved for a wide range of lamellae spacings and temperature. Subsequently, the Fe–C system is examined and the numerical results are compared with experimental data from the literature. Finally, it is shown that the steady-state growth breaks down and the transformation occurs with a different regime at high superheating. © *1998 Acta Metallurgica Inc.*

1. INTRODUCTION

Reaustenitization is the reverse transformation to austenite which occurs in low-alloy steels when the eutectoid temperature is exceeded [1]. For steels in the pearlitic condition, the first step in the transformation is the nucleation of austenite at the interfaces between the pearlite nodules, followed by growth of the austenite into the lamellar structure [2–4]. At temperatures for which the transformation proceeds, the nucleation of austenite occurs very rapidly and the atomic mobilities are usually large enough for austenite growth to be accomplished by diffusional processes [4, 5]. It is likely that growth is controlled by volume—rather than surface—diffusion effects, since the reaction temperature is significantly higher than for pearlite growth. The mean distance over which diffusion occurs is of the order of the interlamellar spacing, which is of course determined not by the reaustenitization reaction itself, but by the kinetics of the eutectoid reaction when the pearlite structure was previously formed [6]. As a consequence, the kinetics of reaustenitization depends mainly upon the scale of the microstructure and composition of the steel under consideration, as well as the magnitudes of the appropriate diffusion coefficients.

At the onset of the reaustenitization reaction from the pearlite structure, the austenite growth rate is a maximum at the places where the diffusion distances are the shortest, i.e. near the lines where the ferrite (α), austenite (γ) and cementite (θ) phases meet. At moderate superheatings, there is however evidence [2] to suggest that a uniform growth velocity or "steady-state" regime is attained, consistent with the net concentration of the pearlite being equivalent to that of austenite far from the transforming region. Therefore, the steady-state dissolution rate of the pearlite must be closely related to the shape of the α/γ and θ/γ interfaces. These depend upon surface tension effects, which influence the thermodynamic equilibrium at the interfaces according to the local curvature via the Gibbs–Thomson effect and also dictates the angle between the interfaces at the lines where the three phases meet.

2. BACKGROUND

The theoretical [4, 5] and experimental [2, 3, 7–9] aspects of reaustenitization kinetics have been widely discussed in the literature. Several numerical models have also been proposed, generally for spheroidized ferrite–cementite microstructures [10–13]. The dissolution of pearlite has received less attention, possibly because of the need to estimate the interphase boundary shapes which are adopted during the transformation. Following Brandt's approach for the eutectoid reaction [14], Speich and

†To whom all correspondence should be addressed.

Szirmae [4] have developed an analytical model for pearlite dissolution kinetics with a simplified solution for the concentration field in austenite. However, severe assumptions were made by these authors: (i) the model accounts only for the first two terms in the Fourier series expressing the concentration field, (ii) the interfacial flux condition is not handled in a consistent manner along the interfaces, and (iii) the interfacial curvature and thus capillarity effects are not treated. These assumptions gave rise to large deviations from experimental results.

In the same paper, the authors proposed a second model giving the pearlite dissolution rate as a function of temperature and interlamellar spacing. Although this simple model is based on a mean diffusion distance only, it gives results which are in better agreement with the experimental data. Hillert *et al.* [5] proposed a similar model which also accounts for the diffusion in the ferrite. More recently, some attempts have been made to solve the problem numerically using a two-dimensional finite difference model [15]. However, the boundary conditions at the moving interface were not explicitly accounted for. It is well established though that two conditions must be imposed at a moving interface whose position is unknown and part of the problem: one is dictated by the equilibrium phase diagram and the second is the solute flux balance.

The purpose of the present paper is to present details of a model describing the transformation process of pearlite into austenite and to show the results of calculations for typical reaustenitization conditions. The problem is solved for a bidimensional geometry characteristic of a regular lamellae structure. The diffusion equation and interfacial boundary conditions are considered in order to estimate the dissolution rate, the shape of the interface as well as the concentration field in austenite as a function of temperature. As will be shown, the model describes both the transient and the steady-state regimes. The model is presented in the next section, whereas the numerical details are given in Appendix A. It is first applied to a model alloy and then to the Fe–C system in Section 4.

3. DETAILS OF THE MODEL

The model describes the growth of the austenitic phase into a lamellar structure of pearlite as illustrated on Fig. 1. It is based upon the equations describing the diffusion of carbon and the displacement of the interface. The following assumptions are made:

- Nucleation of austenite is assumed to occur at the grain boundary between cementite and ferrite. The nucleation overheating is assumed to be zero.
- The microstructure shows a periodicity characterized by a lamellae spacing λ. This assumption reduces the problem to the small domain illustrated on the right-hand side of Fig. 1. This spacing is given by the conditions of pearlite formation on cooling and thus, unlike eutectic or eutectoid models, is not part of the problem.
- The angle β formed by the interfaces at the junction point of the three phases is determined by the mechanical equilibrium of the surface tensions $\sigma_{\gamma/\alpha}$, $\sigma_{\gamma/\theta}$ and $\sigma_{\alpha/\theta}$ (see Fig. 1).
- The carbon concentration in cementite (stoichiometric compound) and in ferrite (very low solubility) is constant during the transformation, so that growth is governed by the volume diffusion of carbon in austenite only.
- The temperature is uniform in the calculation domain. This assumption is justified since the thermal diffusivity is much higher than the solute diffusivity in metals.
- The condition of local equilibrium is applied, so that the carbon concentration at the interfaces can be deduced from the phase diagram for a given temperature modified by the curvature contribution.
- Capillarity is accounted for, via the local curvature modifying the thermodynamic equilibrium. The Gibbs–Thomson coefficient is assumed to be independent of crystallographic orientation.

The problem is thus reduced to the solution of the diffusion equation of carbon in the austenite domain only:

$$\mathrm{div}(D_\gamma \, \mathbf{grad}\, c) + \mathbf{v}_{\mathrm{ref}} \cdot \mathbf{grad}\, c = \frac{\partial c}{\partial t} \qquad (1)$$

where c and D_γ are the concentration field and the diffusion coefficient of carbon in austenite, respectively. The term $\mathbf{v}_{\mathrm{ref}}$ is the velocity of the reference frame with respect to the microstructure. It can be set to zero or taken equal to the mean velocity of the γ/α and γ/θ interfaces.

Under the assumptions made, equation (1) has to be solved for the austenite region with appropriate boundary conditions. At the boundaries of the periodic domain, a zero-flux condition is applied. At the moving γ/α and γ/θ interfaces, whose position and shape are part of the problem, two conditions must be applied. The first one is an essential condition. It involves imposing the interfacial concentrations, $c_{\gamma/\alpha}(T,K)$ and $c_{\gamma/\theta}(T,K)$,† given by the phase diagram modified for the local curvature, K, via the Gibbs–Thomson coefficient:

$$c_{\gamma/\alpha}(T,K) = c^{\infty}_{\gamma/\alpha}(T - \Gamma_{\gamma/\alpha}K) \qquad (2)$$

†The symbol $c_{\gamma/\alpha}$ denotes the interfacial concentration at the γ/α interface in the γ phase.

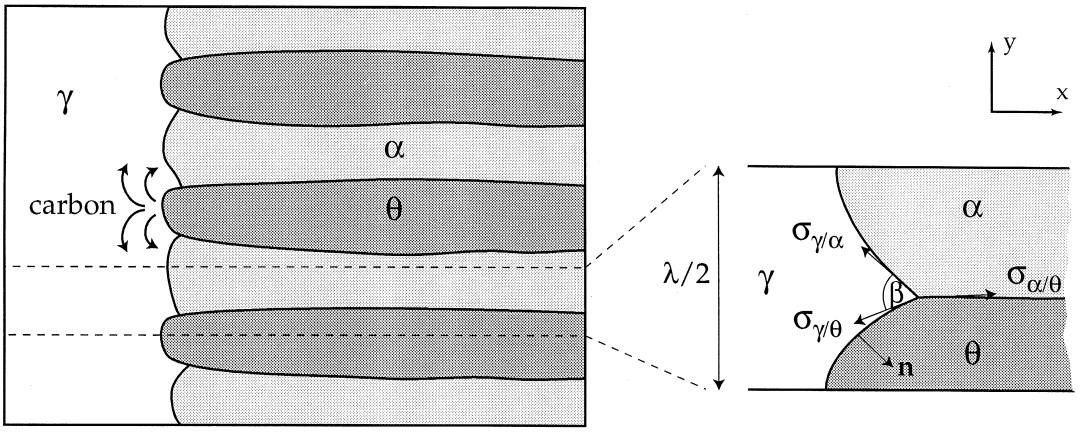

Fig. 1. Schematic representation of the transformation of pearlite into austenite.

$$c_{\gamma/\theta}(T,K) = c^{\infty}_{\gamma/\theta}(T - \Gamma_{\gamma/\theta}K). \tag{3}$$

Here, $c^{\infty}_{\gamma/\alpha}(T)$ and $c^{\infty}_{\gamma/\theta}(T)$ are the concentrations given by the phase diagram for a planar interface at temperature T (see Fig. 2). The curvature K is positive when the γ domain has a convex shape locally and is negative in the case shown in Fig. 2.

The second condition is related to the conservation of carbon fluxes:

$$(D_\gamma \,\mathbf{grad}\, c)_{\gamma/\nu} \cdot \mathbf{n} = \mathbf{v}^{\gamma/\nu} \cdot \mathbf{n}(c_{\nu/\gamma} - c_{\gamma/\nu}) \quad \text{with } \nu = \alpha \text{ or } \theta \tag{4}$$

where $\mathbf{n}$ is the unit vector normal to the interface pointing out of the γ domain (see Fig. 1), $\mathbf{v}^{\gamma/\nu}$ the absolute interface velocity and $(c_{\nu/\gamma} - c_{\gamma/\nu})$ the jump of concentration at the corresponding γ/ν interface (see Fig. 2).

The solution of equation (1) with boundary conditions (2) and (3) is obtained numerically using a finite element method with a deforming mesh and a remeshing procedure. A schematic calculation domain is illustrated on Fig. 3 together with the finite element mesh at two stages of the transformation. The details of the finite element formulation are given in Appendix A.

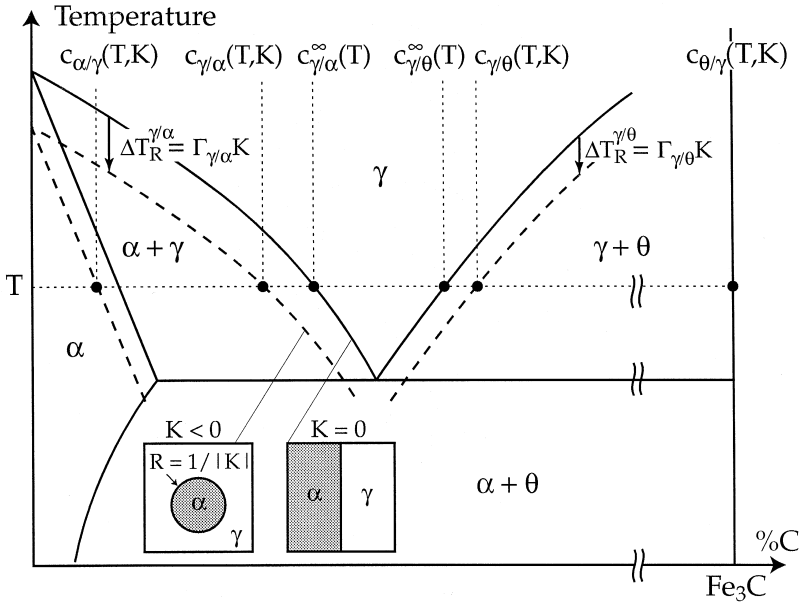

Fig. 2. Definition of the concentrations which are imposed at the interface as boundary conditions of the diffusion problem. Please note that $\Delta T_R^{\gamma/\nu}$ depends on the local curvature of the corresponding interface γ/ν ($\nu = \alpha$ or θ). Therefore it is not the same on the right- and left-hand side of the phase diagram ($K < 0$ for a concave γ/ν interface).

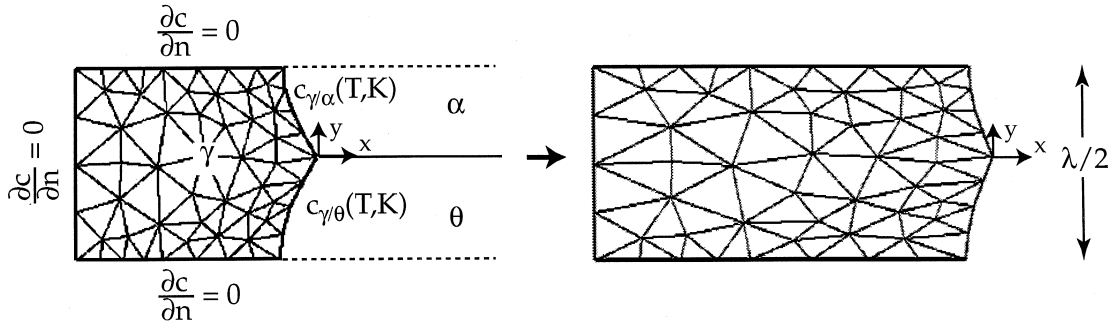

Fig. 3. Calculation domain and boundary conditions used in the model. The finite element mesh is stretched in the x-direction according to the local velocity of the interface.

The concentration field obtained at each time step allows the horizontal velocity of the interface to be deduced from a consideration of equation (4):

$$v_x^{\gamma/\nu} = \frac{D_\gamma}{(c_{\nu/\gamma} - c_{\gamma/\nu})}\left(\left.\frac{\partial c}{\partial x}\right|_{\gamma/\nu} + \frac{n_y}{n_x}\left.\frac{\partial c}{\partial y}\right|_{\gamma/\nu}\right)$$

$$(\text{if } n_x \neq 0),\ \nu = \alpha \text{ or } \theta. \qquad (5)$$

The partial derivatives refer to the two components of the concentration gradient in austenite at the interface, whereas n_x and n_y are the components of the normal vector **n**. The latter is calculated for each interfacial node by averaging the normal vectors of the two neighbouring edges.

From a knowledge of the velocity of the interface, the mesh can be deformed. At each time step the nodes are moved horizontally by a quantity $u_x \Delta t$, where Δt is the time step and u_x the relative velocity. The latter is calculated using the following expression:

$$u_x(x_0,y_0) = \frac{x_0}{x_{\gamma/\nu}(y_0)}(v_x^{\gamma/\nu}(y_0) - v_{ref}) \qquad (6)$$

where (x_0,y_0) are the node coordinates and $x_{\gamma/\nu}(y_0)$ and $v_x^{\gamma/\nu}(y_0)$ refer to the position and the horizontal absolute velocity of the γ/ν interface at ordinate y_0. The nodal point located at the triple point ($\gamma/\alpha/\theta$ junction) and the two neighbours located on each side of it are moved by the same quantity. The latter is estimated by calculating the mean velocity of the two neighbours. This procedure allows the angle β at the interfaces γ/α and γ/θ at the triple point to be maintained during the calculation, consistent with the surface tensions being in mechanical equilibrium. This angle is imposed at the beginning of the calculation by displacing horizontally the nodal point located at the triple point. Accordingly, the initial domain is a very thin rectangular layer with a small cusp at the triple point.

The curvature at each nodal point is estimated from the normal unit vectors of the two neighbouring edges using the following expression:

$$K = \text{div}\, \boldsymbol{n}. \qquad (7)$$

Knowledge of K allows the interfacial concen-

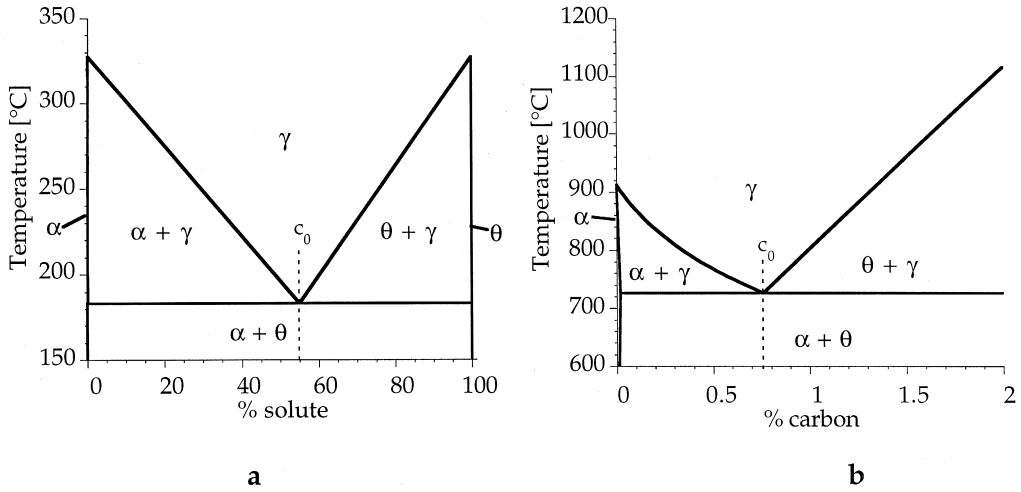

Fig. 4. Phase diagrams used in the calculation for the model alloy (a) and the Fe–C alloy (b).

trations to be updated according to expressions (2) and (3) and enables a new iteration to begin.

Large deformations of the mesh can lead to a degeneration of the elements, and in order to avoid such effects a remeshing procedure is performed as soon as one of the triangular elements exhibits an angle smaller than a given criterion (8°). The new mesh is obtained from the nodal points located on the border of the domain according to a frontal algorithm [16]. The concentration field at the new mesh points is deduced from the shape functions and the concentrations at the previous mesh points.

The operations performed during a time step can be summarized as follows:

1. estimation of the interface curvature (equation (7));

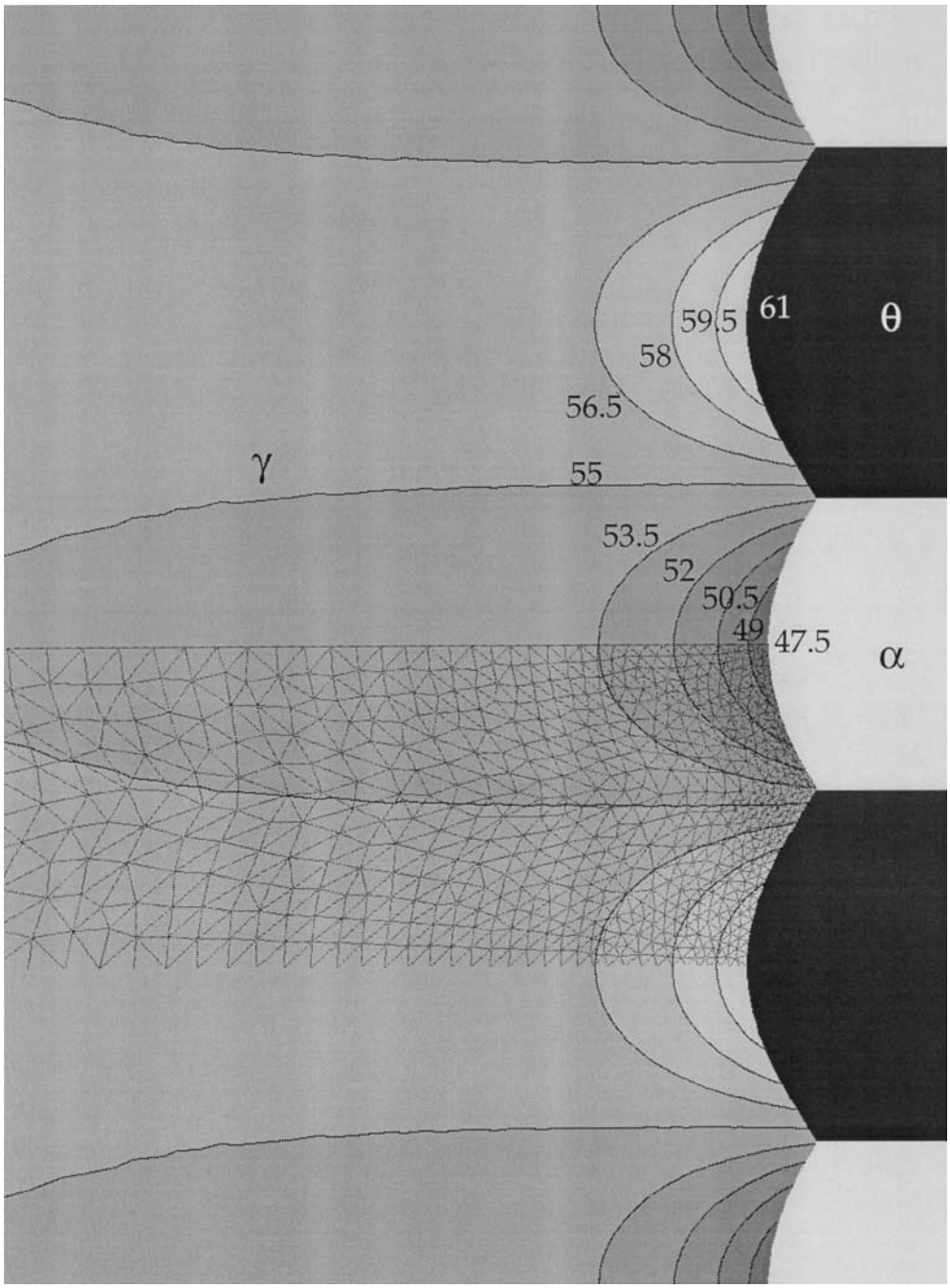

Fig. 5. Concentration field at steady state during the reverse eutectoid transformation for the model alloy ($\lambda = 0.4\ \mu$m, $\Delta T = 3$°C, $\beta = 120$°, $D_\gamma = 3 \times 10^{-10}$ m^2/s, 926 nodes, CPU time (HP-PA8000 workstation): 15 min).

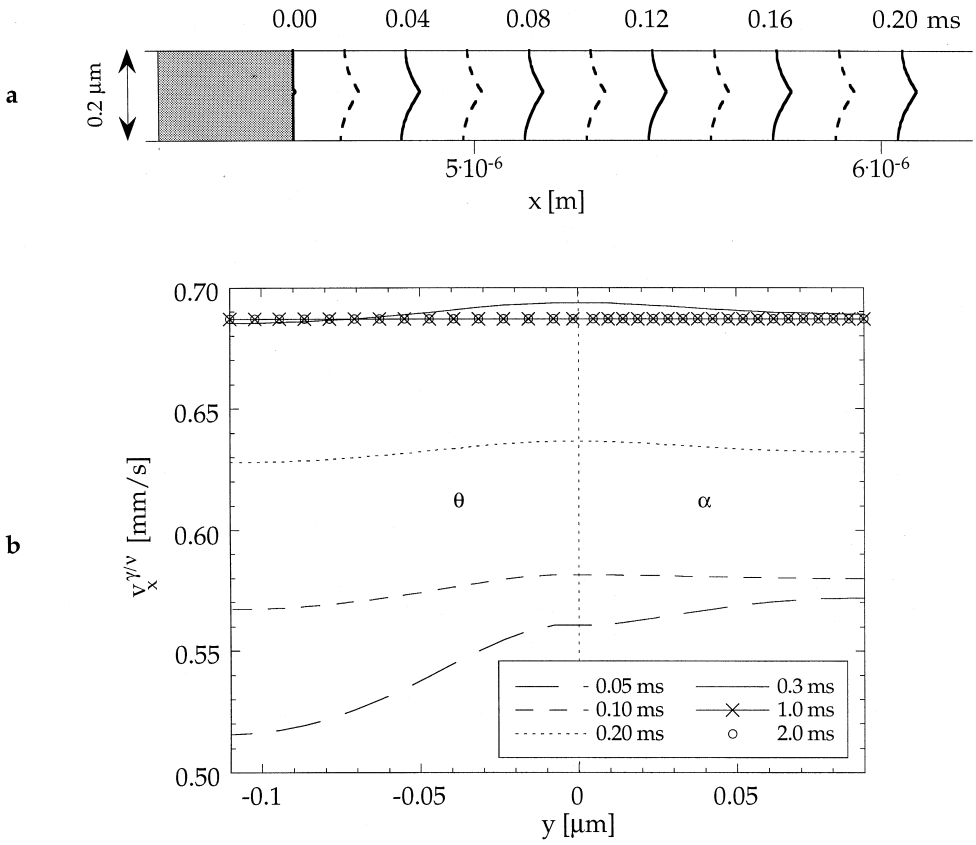

Fig. 6. Position of the interface (a) and velocity profile (b) at different times during the transformation of the model alloy (same conditions as in Fig. 5).

2. calculation of the concentration field in the actual domain by solving equation (1) with boundary conditions (2) and (3);
3. calculation of interfacial node velocities (equation (5));
4. update the position of the nodes (equation (6));
5. remeshing (if necessary).

4. RESULTS AND DISCUSSION

4.1. Application to a model alloy

Prior to the application of the model to the austenitization problem, a number of numerical tests were carried out in order to validate the formulation, to check for the presence of numerical errors

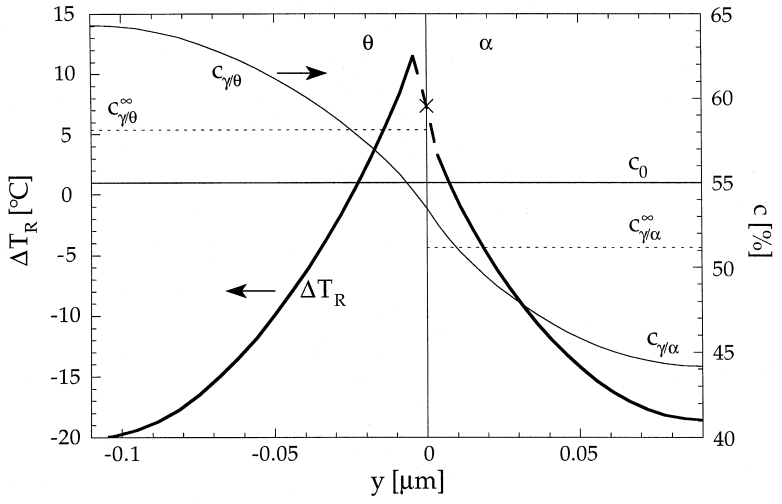

Fig. 7. Curvature overheating and carbon concentration in austenite at the interface for the model alloy at steady state ($\lambda = 0.4\ \mu$m, $\Delta T = 10$°C, $\beta = 120$°). c_0 is the eutectoid concentration.

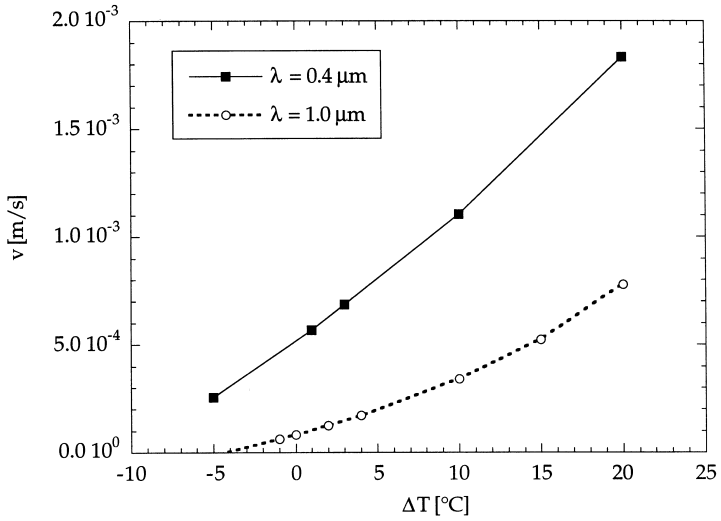

Fig. 8. Steady-state dissolution rate vs overheating calculated for two interlamellar spacings of the model alloy.

associated with the deformation of the mesh and finally to assess the accuracy of the numerical formulation [17]. For the specific situations tested, it was found that the scheme was quite accurate and did not introduce significant errors.

A model alloy has been used for studying the behaviour of the model when the different parameters are changed. The physical properties of this alloy have been chosen in order to avoid the case of microstructures showing α lamellae which are much thicker than the θ lamellae. The phase diagram was thus almost symmetric with a eutectoid composition fixed at 55% (see Fig. 4(a)). The diffusion coefficient, the Gibbs–Thomson coefficient and the angle β were set to 3×10^{-10} m^2/s, 2×10^{-6} m K and 120°, respectively.

The set of axes was attached to the triple point. Its velocity, v_{ref}, which is not constant during the transformation, was recorded during the entire calculation in order to be able to reconstruct the displacement. The resolution was pursued until a steady state was reached (constant shape of the γ/α and γ/θ interfaces). The calculations were performed with an overheating varying between -5 and $+20$°C. The use of negative values will be justified further in the text.

The concentration field obtained at steady state is shown on Fig. 5 for a 3°C overheating and a 0.4 μm interlamellar spacing. The calculations were performed in the domain illustrated by the FE mesh and the full picture was obtained using two operations of symmetry. The numbers correspond to various isopleths of the concentration field. As can be seen, the concentration gradient in the γ phase along a given γ/v interface is fairly constant. This allows the whole interface to move with a constant velocity along the x-axis, regardless of the ordinate y. The achievement of a steady state is demonstrated on Fig. 6 where the position of the interface and the horizontal velocity have been plotted as a function of time. It can be deduced that the duration of the initial transient is about 0.3 ms and that the steady-state velocity is 0.69 mm/s under such conditions.

The fact that the concentration gradient along an interface is fairly constant regardless of its distance to the triple point can be found in the curvature contribution: near the triple point, where the diffusion distance is short, the concentration difference between the two interfaces is greatly reduced by the high positive curvature, whereas the opposite occurs in the regions far from the triple point. The effect of the local curvature on the thermodynamic equilibrium is shown on Fig. 7 for a 10°C overheating. The curvature contribution to the overheating, $\Delta T_R = \Gamma K$, plotted as a function of the ordinate y of the interface allows the overheating available for diffusion, ΔT_c, to be deduced:

$$\Delta T_c = T - T_{eut} - \Gamma K = \Delta T - \Delta T_R \qquad (8)$$

where ΔT is the imposed value of overheating ($\Delta T = T - T_{eut}$), T the transformation temperature and T_{eut} the eutectoid temperature for a planar interface. Note that the curvature contribution, ΔT_R, at the triple point is ill-defined and has been obtained by averaging the curvature contributions at the two neighbouring interfacial nodes. Figure 7 shows that the diffusion overheating near the triple point ($y = 0$) is considerably reduced by the positive curvature. (It can even be slightly negative.) On the other hand, near the centre of the lamellae, the interface has a negative curvature which increases the diffusion overheating and thus compensates for the longer diffusion distance. The interfacial concen-

trations, $c_{\gamma/\alpha}(T,K)$ and $c_{\gamma/\theta}(T,K)$, deduced from the phase diagram modified for the local curvature K, have also been represented on Fig. 7. As can be seen, $c_{\gamma/\alpha}$ and $c_{\gamma/\theta}$ vary continuously along the interface and show large deviations from the values for a planar interface, $c^{\infty}_{\gamma/\alpha}$ and $c^{\infty}_{\gamma/\theta}$ (dashed horizontal lines). This result emphasizes the importance of the curvature effects in the dissolution process.

The steady-state transformation rates obtained at various overheatings have been represented on Fig. 8 for two interlamellar spacings. The positive dissolution rate observed for the negative values of overheating is due to the mechanical equilibrium which is imposed at the junction point. From the beginning of the calculation, the austenitic domain has a concave shape which enhances the dissolution by a diminution of the equilibrium temperature. As expected, the dissolution rate increases with the overheating and decreases with the interlamellar spacing. The v(ΔT) relationship is almost linear with a slight increase of the slope at high overheating.

4.2. *Application to the Fe–C alloy*

The model has been applied to the pearlite dissolution using more realistic physical properties for the Fe–C alloy. The phase diagram used for the calculation is illustrated on Fig. 4(b). The other numerical data were $\lambda = 0.5\ \mu$m, $D_\gamma = 1.4 \times 10^{-12}$ m^2/s, $\Gamma_{\gamma/\alpha} = \Gamma_{\gamma/\theta} = 2 \times 10^{-7}$°C m. The calculations were performed with a Gibbs–Thomson coefficient $\Gamma_{\alpha/\theta}$ varying between 0.1×10^{-7} and 2×10^{-7}°C m.† This allowed the influence of the angle β ($177° > \beta > 120°$) on the dissolution kinetics to be studied. The nominal composition was taken equal to the eutectoid concentration, $c_0 = 0.761\%$, for all calculations.

The concentration field in austenite at steady state for $\Delta T = 1$°C and $\beta = 166°$ is shown on Fig. 9. The numbers correspond to various isopleths of the carbon concentration field. As can be seen, the concentration gradient along a given interface is fairly constant, regardless of the distance to the triple point. This is due again to the curvature contribution and ensures a steady state.

Similar calculations were made using different values of β in the range 120°–177° and the same conditions ($\Delta T = 1$°C, $\lambda = 0.5\ \mu$m). The results are shown on Fig. 10 where the steady dissolution rate and the interface shape are plotted as a function of β. As can be seen, the influence of the angle β is strong. The dissolution rate is reduced by a factor of 2 when β varies from 120° to 177°. A small angle β induces a hollow-shaped interface which increases the concentration gradient and makes the curvature more negative near the centre of the lamellae. The diffusion rate and the effective concentration difference between the γ/θ and γ/α interfaces are much higher in that case and consequently the dissolution rate is faster than for a flat interface.

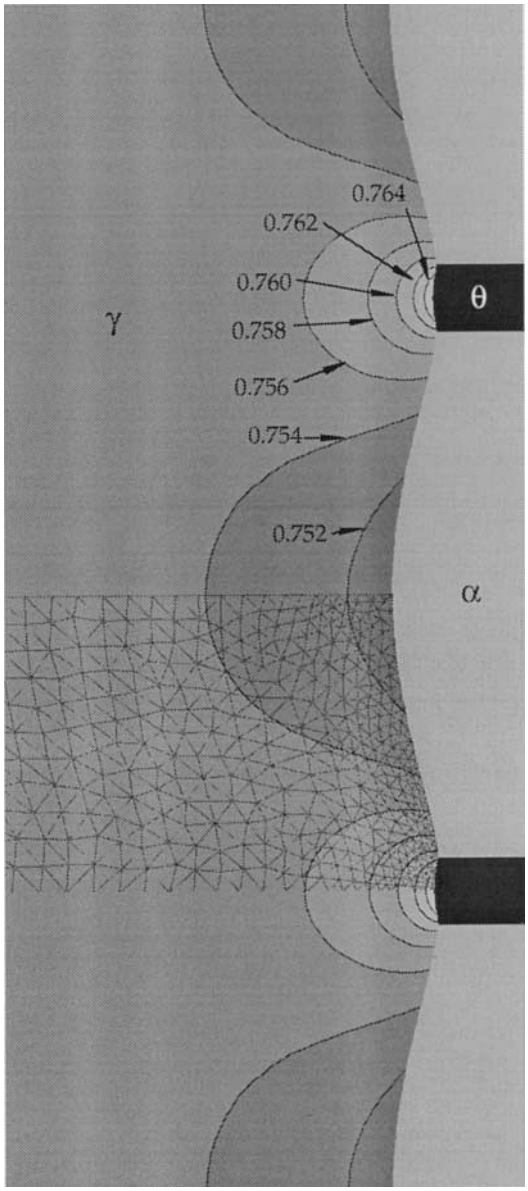

Fig. 9. Carbon concentration field in austenite during the steady-state dissolution of a pearlitic microstructure ($\lambda = 0.5\ \mu$m, $\Delta T = 1$°C, $\beta = 166°$, $D_\gamma = 1.4 \times 10^{-12}$ m^2/s, 1075 nodes, CPU time: 9 h).

The steady-state dissolution rates obtained with two different values of β have been represented on Fig. 11 as a function of overheating. The results are compared with experimental data extracted from literature for a eutectoid steel showing a similar pearlite spacing [2]. The predicted dissolution rates are in good agreement with the experimental one. The values obtained with a 120° angle are, however,

†$\Gamma_{\alpha/\theta}$, $\Gamma_{\gamma/\alpha}$ and $\Gamma_{\gamma/\theta}$ were estimated according to Kramer *et al.*'s work [18] and other values for solidification [19].

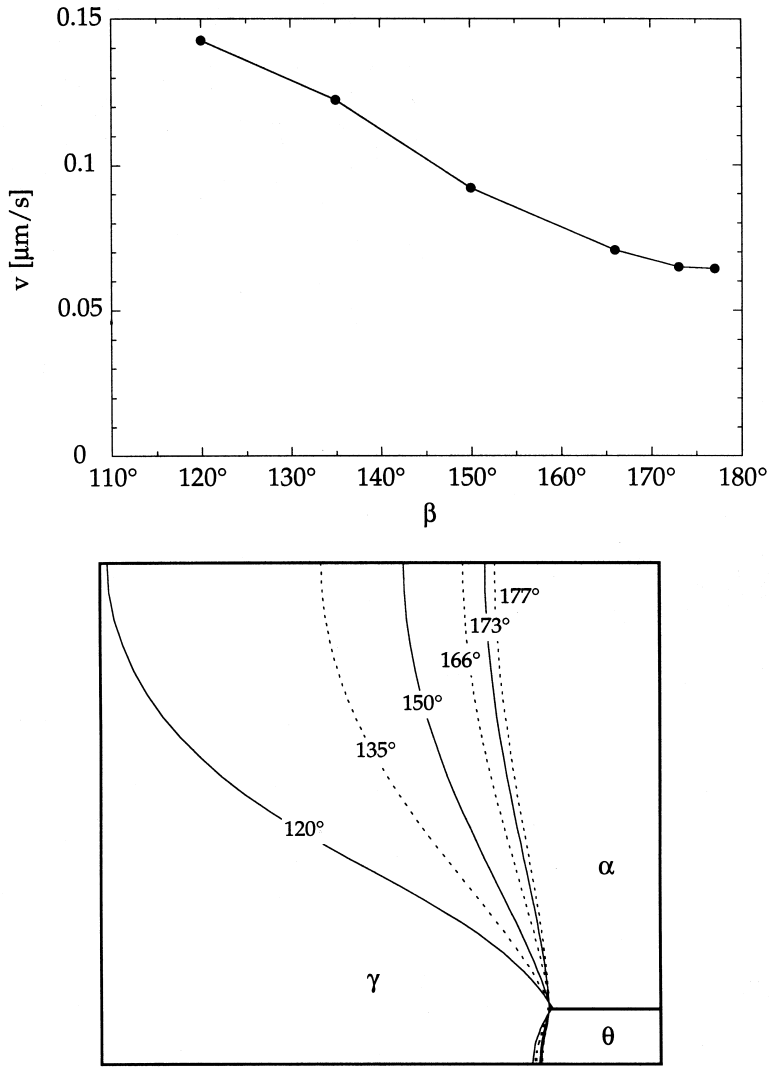

Fig. 10. Steady-state dissolution rate (a) and interface shape (b) during the dissolution of pearlite as a function of the angle β at the triple point ($\lambda = 0.5\ \mu$m, $\Delta T = 1$°C).

slightly too high. This result indicates that the angle is probably closer to 166° than to 120°. This assumption seems to be confirmed by the micrography of Fig. 12 showing an austenitic nodule growing in a pearlitic matrix: the interface between austenite and pearlite is observed to be quite smooth [2]. For reasons which are given below, converged steady-state FEM results could not be obtained for the Fe–C system beyond an overheating of 3°C. Therefore, comparison with the experimental results of [2] could only be made over a small overheating range in Fig. 11.

The simulation results have also been compared in Fig. 11 with the solution of Speich and Szirmae's analytical model which was mentioned in Section 2 [4]. The concentration field given by this analytical solution, which consists of an approximate solution of the diffusion equation, has been plotted on Fig. 13. The parameters used are the same as those of Fig. 9 ($\lambda = 0.5\ \mu$m, $\Delta T = 1$°C) so that a direct comparison between the two figures is possible. In the analytical model, the shape of the interface is given by the isopleths $c^{\infty}_{\gamma/\alpha}$ (0.754%) and $c^{\infty}_{\gamma/\theta}$ (0.764%) of the concentration field. Those lines mark the boundary of the α and θ regions (white) on Fig. 13. The relative depth of the α and θ lamellae which are obtained with the analytical model are very different from those given by the phase diagram and used in the numerical model. This difference is due to the use of a second-order solution only, which is too approximate to describe properly the concentration gradient together with a correct lamellar depth. Moreover, the curvature contribution is totally neglected in the analytical model. These severe limitations lead to dissolution

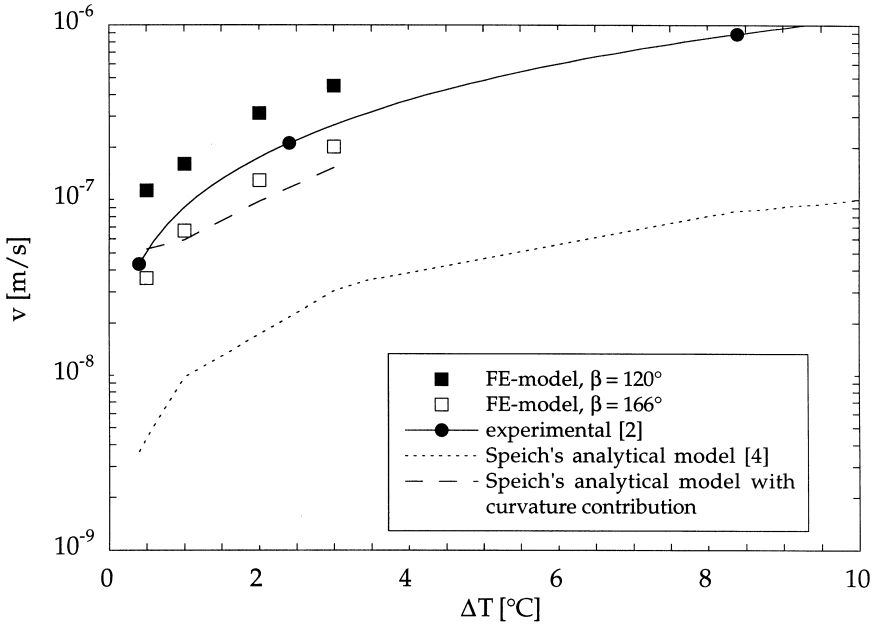

Fig. 11. Steady-state dissolution rate of a pearlitic microstructure as a function of the overheating (Fe–C alloy, $\lambda = 0.5\,\mu$m) for two values of the angle β. Values extracted from Roberts and Mehl's experimental work [2] and results of Speich and Szirmae's analytical model [4] are also represented. The second analytical result is also based upon Speich and Szirmae's approximation but the concentrations at the centre of the lamellae were taken from the FE model for $\beta = 120°$ (i.e. the curvature contribution is included).

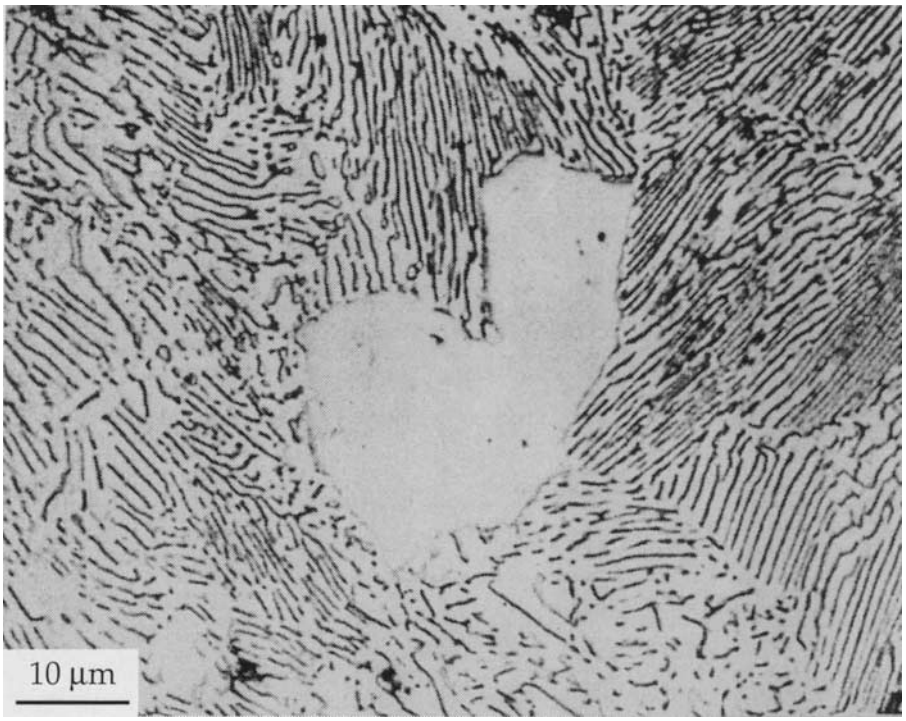

Fig. 12. Austenite nodule growing at the interface between two pearlite colonies in a eutectoid steel [2].

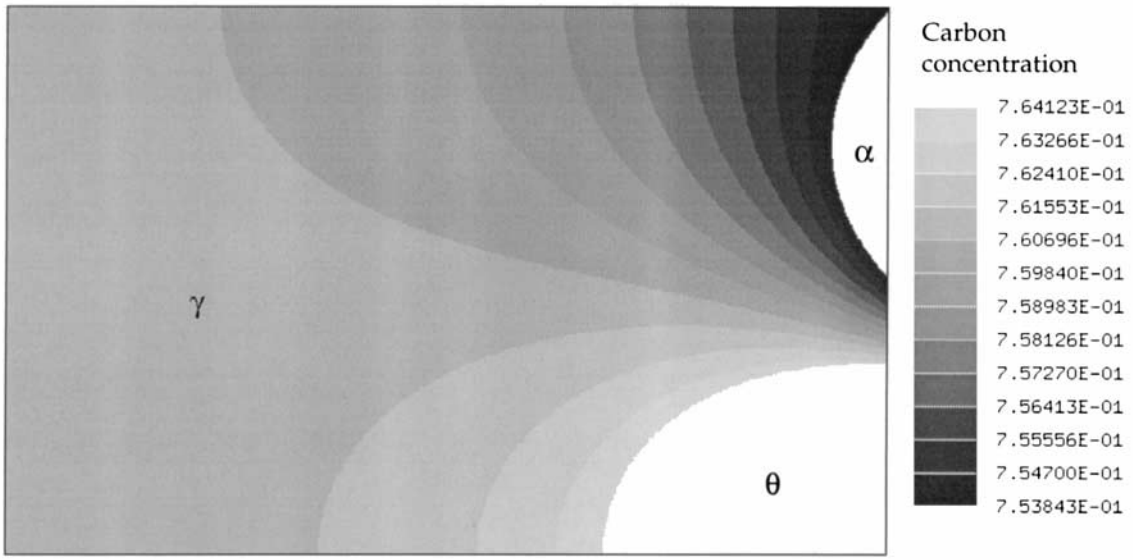

Fig. 13. Concentration field obtained with Speich and Szirmae's analytical model [4] ($\Delta T = 1°C$, $\lambda = 0.5\ \mu m$, $D_\gamma = 1.4 \times 10^{-12}\ m^2/s$).

kinetics which are much lower than the numerical and experimental values (see Fig. 11).

In order to estimate the error associated with the ignorance of the curvature term, the analytical model of Speich and Szirmae was then applied using as a boundary condition the interfacial concentrations $c_{\gamma/\alpha}$ and $c_{\gamma/\theta}$ obtained with the numerical model for the nodes located at the centre of the lamellae (upper and lower right edges of the calculation domain) and $\beta = 120°$. These values, which account for the curvature effects since they are functions of the local curvature in the FE model, were used as boundary conditions of the analytical diffusion model. As can be seen on Fig. 11, the analytical dissolution kinetics obtained under such conditions is in better agreement with the experimental data than the kinetics of the original analytical model. This result demonstrates again the importance of considering the capillarity effects in a diffusion model describing pearlite dissolution.

The concentration field obtained with the numerical model for a higher value of overheating ($\Delta T = 5°C$) is shown on Fig. 14. The steady state was not reached for this calculation because of a degeneration of the mesh. The rapid growth in the region of the triple point at the beginning of the transformation leads to very hollow interfaces and to almost horizontal segments on the γ/θ boundary. The deformation procedure of the mesh, which is based on horizontal displacements only, does not allow such a geometry to be handled and the calculation had thus to be stopped.

The numerical problem and the shape of the interface observed at large overheating seem to indicate that the transformation can proceed according to another regime. This regime would consist of a rapid transformation of the α phase, after which residual cementite lamellae would remain in the austenitic matrix. The dissolution of these carbides would occur later on by a mechanism of lateral diffusion. The difference between the transformation regimes at low and high overheatings is illustrated on Fig. 15. The second regime (Fig. 15(b)) has been predicted by Hillert *et al.* [5] and observed experimentally for coarse pearlitic microstructures (Fig. 16) [20]. Under such conditions, Akbay *et al.*'s one-dimensional growth model [12] is probably more appropriate than the present one.

The transition from one regime to the other is probably associated with the typical length scales for the diffusion and microstructure. As the overheating increases, the diffusion layer in austenite ahead of the interfaces decreases. If it becomes smaller than the interlamellar spacing, the lateral exchange of carbon may not be sufficient for a steady state to be achieved and the second regime will take place.

5. CONCLUSION

A new two-dimensional FEM model has been used to describe in a realistic way the dissolution mechanisms of a eutectoid lamellar microstructure. The dissolution rate, the shape of the interface and the concentration field in austenite have been calculated for the initial transient and for the steady state. Compared with the former analytical models, it provides several improvements, in particular the consideration of the surface tension effects and the prediction of the interface shape. The model has

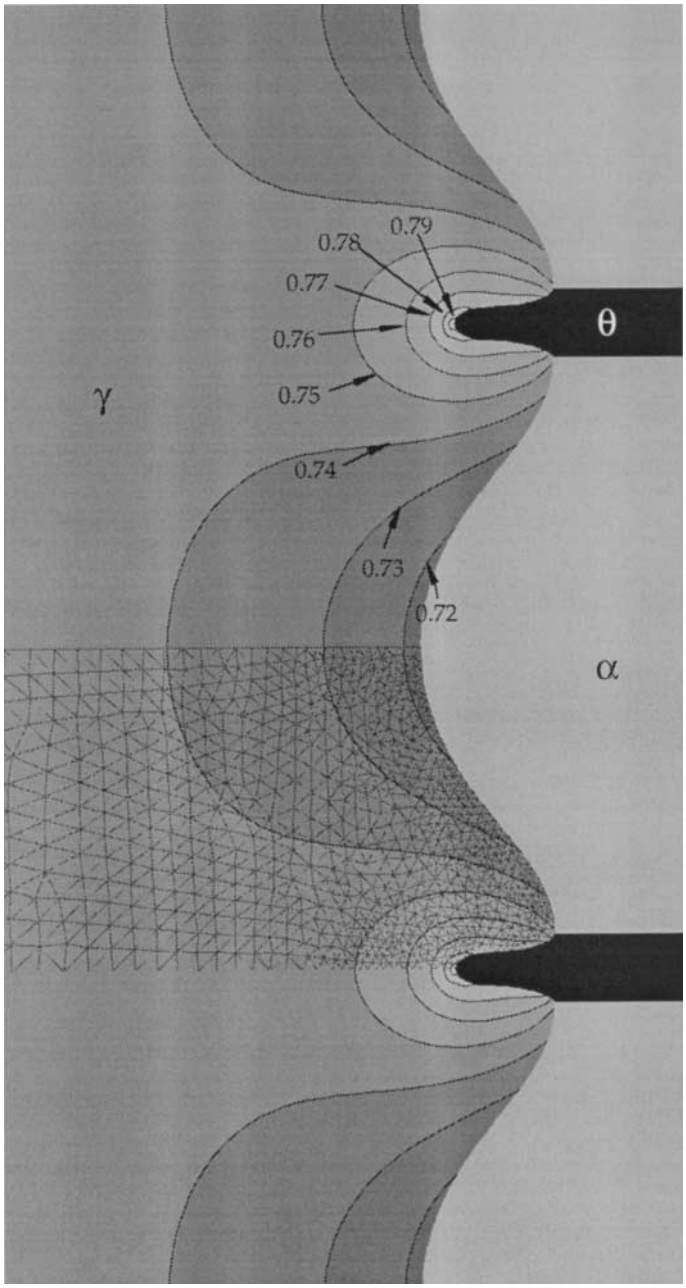

Fig. 14. Non-steady-state concentration field obtained with the FEM model for a 5°C overheating ($\beta = 166°$, $\lambda = 0.5\ \mu$m, $D_\gamma = 1.4 \times 10^{-12}$ m^2/s, $t = 0.12$ s).

been applied successfully to the Fe–C alloy for small values of overheating (less than 3°C). The dissolution rates are in good agreement with the experimental values from the literature.

However, the model did not allow the transformation at higher overheating to be described. Under such conditions, the transformation is likely to proceed with a different regime which involves a rapid dissolution of the ferrite followed by a lateral dissolution of the residual cementite in the austenitic matrix. Further investigations would be needed in order to confirm the existence of this regime and to better understand the transition from one regime to the other. This would however require the modification of the front tracking algorithm used in the present study. On the other hand, the present model could be applied to the remelting of a eutectic microstructure without any modification.

A better knowledge of the physical properties would allow more realistic pearlite dissolution rates to be obtained. Moreover, in order to estimate the total dissolution time of a pearlitic microstructure,

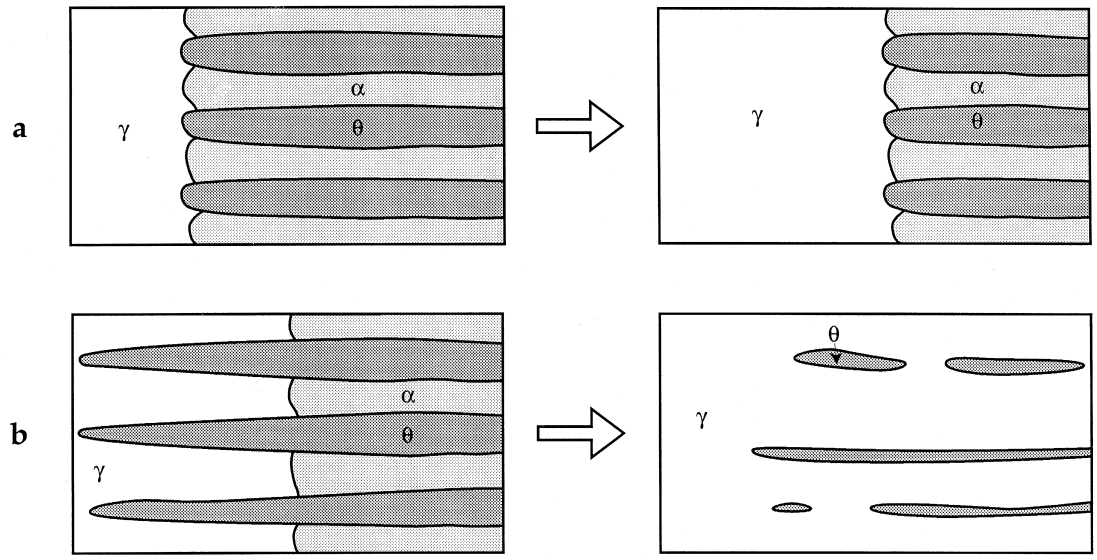

Fig. 15. Presumed dissolution regimes of a pearlitic microstructure: coupled regime at low overheating (a) and non-coupled regime at high overheating (b).

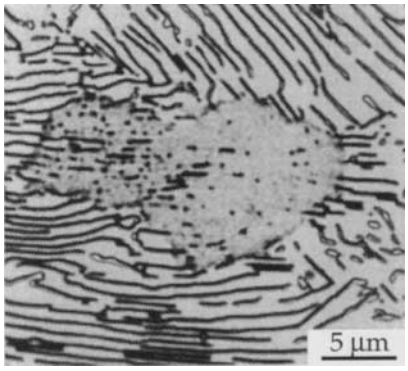

Fig. 16. Microstructure showing the formation of austenite in pearlite (after 26 s at 730°C) [20].

the nucleation phenomena should also be considered. In spite of these limitations, the model allowed the understanding of the dissolution mechanisms to be improved, in particular the importance of the curvature effect and the possible existence of two dissolution regimes.

REFERENCES

1. Brooks, C. R., *Principles of the Austenitization of Steels*. Elsevier Applied Science, London, 1992.
2. Roberts, G. A. and Mehl, R. F., *Trans. ASM*, 1943, **31**(9), 613.
3. Garcia, C. I. and Deardo, A. J., *Met. Trans.*, 1981, **12A**, 521.
4. Speich, G. R. and Szirmae, A., *Trans. TMS of AIME*, 1969, **245**, 1063.
5. Hillert, M., Nilsson, K. and Törndahl, L. E., *J. Iron Steel Inst.*, 1971, **209**, 49.
6. Puls, M. P. and Kirkaldy, J. S., *Met. Trans.*, 1972, **3**, 2777.
7. Molinder, G., *Acta metall.*, 1956, **4**, 565.
8. Rose, A. and Strassburg, W., *Stahl und Eisen*, 1956, **76**, 976.
9. Speich, G. R., Demarest, V. A. and Miller, R. L., *Met. Trans. A*, 1981, **12A**, 1419.
10. Judd, R. R. and Paxton, H. W., *Trans. TMS of AIME*, 1968, **242**, 206.
11. Karlsson, B. and Larsson, L. E., *Mater. Sci. Engng*, 1975, **20**, 161.
12. Akbay, T., Reed, R. C. and Atkinson, C., *Acta metall.*, 1994, **47**, 1469.
13. Atkinson, C., Akbay, T. and Reed, R. C., *Acta metall.*, 1995, **43**, 2013.
14. Brandt, W. H., *J. appl. Phys.*, 1945, **16**, 139.
15. Inoue, K., Ohmura, E. and Ikuta, S., *Trans. of JWRI*, 1987, **16**, 97.
16. Bernadou, M. *et al.*, *Modulef, une bibliothèque modulaire d'éléments finis*. Institut National de Recherche en Informatique, Paris, 1985.
17. Jacot, A., Ph.D. thesis No. 1679, Ecole Polytechnique Fédérale de Lausanne, Switzerland, 1997.
18. Kramer, J. J., Pound, G. M. and Mehl, R. F., *Acta metall.*, 1958, **6**, 763.
19. Kurz, W. and Fisher, D. J., *Fundamentals of Solidification*. Trans Tech Publications, Aedermannsdorf, Switzerland, 1989.
20. Samuels, L. E., *Optical Micrography of Carbon Steels*. American Society for Metals, Metals Park, Ohio, 1980.
21. Lynch, D. R., *J. Comput. Phys.*, 1982, **47**, 387.

APPENDIX A

The finite element formulation is based on a set of shape functions, $\phi_i(\mathbf{x},t)$, which allow the concentration field to be expressed by linear combinations:

$$c(\mathbf{x},t) = \sum_{i=1}^{N} c_i(t)\phi_i(\mathbf{x},t) \qquad \text{(A1)}$$

where c_i is the concentration at node i and N is the total number of nodal points. The time dependence of the shape functions is specific to the procedure of mesh deformation [21]. Multiplying equation (1) by a test func-

tion ϕ_j, integrating over the calculation domain Ω and applying the Orstrogradsky theorem gives:

$$\int_\Gamma D\,\mathbf{grad}\,c\cdot\mathbf{n}\phi_j\,\mathrm{d}\Gamma-\int_\Omega D(\mathbf{grad}\,c\cdot\mathbf{grad}\,\phi_j)\,\mathrm{d}\Omega+\int_\Omega(\mathbf{v}_{\mathrm{ref}}\cdot\mathbf{grad}\,c)\phi_j\,\mathrm{d}\Omega=\int_\Omega\frac{\partial c}{\partial t}\phi_j\,\mathrm{d}\Omega. \tag{A2}$$

The discretization and assembling procedure yields the following matrix equation:

$$\mathbf{b}+([\mathbf{V}_{\mathrm{ref}}]-[\mathbf{D}])\mathbf{c}=[\mathbf{M}]\frac{\mathrm{d}\mathbf{c}}{\mathrm{d}t}+[\mathbf{U}]\mathbf{c} \tag{A3}$$

with

$$b_j=\int_\Gamma D(\mathbf{grad}\,c\phi_j)\cdot\mathbf{n}\,\mathrm{d}\Gamma \tag{A4}$$

$$D_{ji}=\int_\Omega D(\mathbf{grad}\,\phi_i\cdot\mathbf{grad}\,\phi_j)\,\mathrm{d}\Omega \tag{A5}$$

$$M_{ji}=\int_\Omega(\phi_i\phi_j)\,\mathrm{d}\Omega \tag{A6}$$

$$V_{\mathrm{ref},ji}=\int_\Omega(\mathbf{v}_{\mathrm{ref}}\cdot\mathbf{grad}\,\phi_i)\phi_j\,\mathrm{d}\Omega \tag{A7}$$

$$U_{ji}=\int_\Omega\left(\frac{\partial\phi_i}{\partial t}\phi_j\right)\mathrm{d}\Omega. \tag{A8}$$

Introducing in equation (A8) the following expression [21]:

$$\frac{\partial\phi_i}{\partial t}=-\mathbf{grad}\,\phi_i\cdot\mathbf{u} \tag{A9}$$

where $\mathbf{u}$ is the relative velocity of the nodes in a deforming mesh, the matrix equation (A3) can be rewritten as:

$$\mathbf{b}+([\mathbf{V}]-[\mathbf{D}])\mathbf{c}=[\mathbf{M}]\frac{\mathrm{d}\mathbf{c}}{\mathrm{d}t} \tag{A10}$$

with

$$V_{ji}=\int_\Omega((\mathbf{v}_{\mathrm{ref}}+\mathbf{u})\cdot\mathbf{grad}\,\phi_i)\phi_j\,\mathrm{d}\Omega. \tag{A11}$$

In the model the y-component of the velocity is always zero. In addition the velocity can be expressed by the following combination of shape functions:

$$u_x=\sum_{k=1}^{N}u_{x,k}\phi_k. \tag{A12}$$

Since the coordinate system also moves horizontally, equation (A11) can be rewritten as:

$$V_{ji}=\sum_{k=1}^{N}(v_{\mathrm{ref}}+u_k)\int_\Omega\frac{\partial\phi_i}{\partial x}\phi_j\phi_k\,\mathrm{d}\Omega. \tag{A13}$$

The solution of equation (A10) is estimated with the following explicit scheme:

$$\mathbf{b}+([\mathbf{V}]-[\mathbf{D}])\mathbf{c}^t=[\mathbf{M}]\frac{\mathbf{c}^{t+\Delta t}-\mathbf{c}^t}{\Delta t}. \tag{A14}$$

The time step Δt is determined with the stability criterion for an explicit scheme and a lumped mass matrix:

$$\Delta t<\frac{1}{4}\left(\frac{L^2}{D}\right)_{\min} \tag{A15}$$

where $(L^2/D)_{\min}$ is the minimum over the entire domain of the ratio given by the edge length, L (minimum of the three edges for each element) and the diffusion coefficient D calculated as a function of the local concentration.